Science of the Total Environment 669 (2019) 322–332

Contents lists available at ScienceDirect

Science of the Total Environment

journal homepage: www.elsevier.com/locate/scitotenv

On the interactions between airflow and ice melting in ice caves: A novel methodology based on computational fluid dynamics modeling

Barbara Bertozzi[a], Beatrice Pulvirenti[b,*], Renato R. Colucci[c,d], Silvana Di Sabatino[e]

[a]Institute of Meteorology and Climate Research - Karlsruhe Institute of Technology, Karlsruhe, Germany
[b]Department of Industrial Engineering - University of Bologna, Italy
[c]Department of Earth System Sciences and Environmental Technology - ISMAR, CNR Trieste, Italy
[d]E. Boegan Cave Commission, Società Alpina delle Giulie Trieste, Italy
[e]Department of Physics and Astronomy - University of Bologna, Italy

HIGHLIGHTS

- The distribution and the volume of ground ice in Alpine caves remain still unknown
- In ice caves the airflow is often induced by temperature differences
- Airflows within the ice cave locally modify the energy balance
- The heat transfer with air is connected to the mass balance of perennial ice deposits
- Climate change affects the level of ice within ice caves

GRAPHICAL ABSTRACT

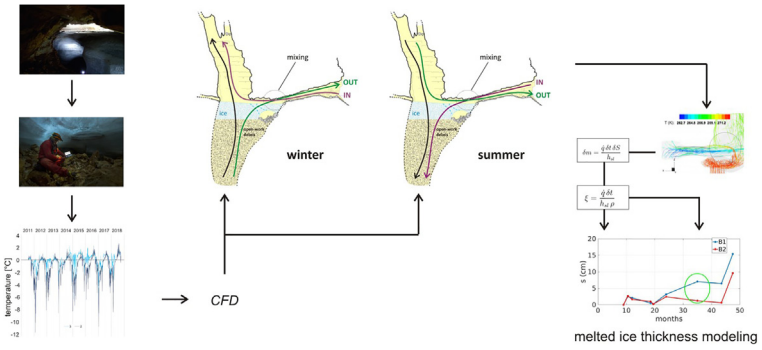

ARTICLE INFO

Article history:
Received 11 October 2018
Received in revised form 2 March 2019
Accepted 5 March 2019
Available online 9 March 2019

Editor: José Virgílio Cruz

Keywords:
Ice cave
CFD approach
Heat transfer
Ice melting
Climate change

ABSTRACT

Motivated by progressive climate-change influence on ice degradation in caves, in this paper we present a novel methodology to investigate the link between air dynamics and ice melting. Specifically, we use surveys available for the Leupa ice cave (LIC), located in the Canin-Kanin group in the southeastern Alps and a general purpose computational fluid dynamics model (CFD). Detailed numerical simulations are evaluated on the basis of well-established approaches that consider domain, grid, boundary-conditions, turbulence closure models, buoyancy effects, porous media properties and verification with measured data. External atmospheric conditions are the main trigger for internal circulation but morphology and thermal characteristics of ice and bedrock induce a dynamical process of heat exchange ultimately responsible for ice melting. This process is generally poorly documented in real conditions. Using CFD analyses we show that both in summer and winter, warm and cold air currents within the cave are "disturbed" by several vortices and stagnation zones which locally modify the energy balance. To account for this we introduce a macroscopic physical model based on energy balance between ice surfaces and the inner ice cave airflow to determine the heat exchanged between ice and air. Using this model, a prediction of ice thickness decay over time is obtained. In the case of LIC a reduction of initial 4 cm per year is first obtained with projection of a much faster increase. The methodology is general and easily extendable to other sites, proving to be a powerful method to estimate ice evolution in caves induced by external and internal forcing.

© 2019 Elsevier B.V. All rights reserved.

* Corresponding author.
E-mail address: beatrice.pulvirenti@unibo.it (B. Pulvirenti).

https://doi.org/10.1016/j.scitotenv.2019.03.074
0048-9697/© 2019 Elsevier B.V. All rights reserved.

1. Introduction

A lesser known part of the alpine cryosphere is currently represented by alpine ice caves, namely natural caves formed in bedrock (karstic massifs and lava tubes) where perennial accumulation of ice is preserved (Perşoiu and Onac (2012)) (Perşoiu and Onac, 2012). Ice caves are part of the permafrost phenomena (e.g., Luetscher et al. (2005), Luetscher et al. (2013), Hausmann et al. (2011), Kern et al. (2011), Colucci et al. (2017)) being characterized by permanent (more than two years) ground ice deposits. The distribution and the volume of ground ice in Alpine caves remain stillstill remain unknown, although recent studies (e.g. Maggi et al. (2018), Oliva et al. (2018)) suggest that the number of ice caves in the Alps could reach several thousands of units, thus representing a possible important source of freshwater storage in high altitude karstic areas (Colucci et al. (2016)) (Colucci et al., 2016). Ice caves are generally located at elevations higher than 1000 m asl in the European Alps, therefore also being reported in environments where the mean annual air temperature (MAAT) is well above 0°C (Holmlund et al. (2005), Stoffel et al. (2009), Obleitner and Spotl (2011), Spötl and Cheng (2014), Colucci et al. (2016)). In the southeastern Alps ice caves generally form where the mean summer air temperature is below the 13°C threshold, and the mean winter air temperature is less than -2–2 °C. With MAAT < 2°C their number rapidly increases (Colucci et al. (2016)) (Colucci et al., 2016). Cave microclimate is generally described according to its thermodynamic characteristics (Luetscher and Jeannin (2004)) (Luetscher and Jeannin, 2004). Also, the presence of entrances is to be considered in the assessment of ice caves micro-climate given that they represent corridors for exchanging warm and cold air with the external atmosphere. Different mechanisms lead to ice formation: i) recrystallization of snow; ii) refreezing of percolating water; iii) sublimation and deposition of cave-air vapor (Luetscher and Jeannin (2004)) (Luetscher and Jeannin, 2004). Ice degradation processes in caves are widely observed all over the world (e.g., Luetscher et al. (2005), Behm et al. (2009), Colucci et al. (2016)) and for this reason it is extremely important and urgent the understanding of processes involved in such rapid evolution is extremely important and urgent. Moreover, little is known about the processes controlling the mass balance of perennial sub-surface ice deposits and its evolution under changing climate conditions (Luetscher et al. (2008)) (Luetscher et al., 2008). Great attention has been lately dedicated to the possible existence of cave ice deposits on Mars owing to the importance of such environments as potential reservoirs of stable or metastable water-ice deposits, which could be an invaluable resource in Mars exploration and future settlements (Frederick et al. (2000)) (Frederick et al., 2000). Williams et al. (2010) recently modeled cave-ice deposition and stability for various locations on Mars, concluding that subsurface water-ice can exist for long periods across much of the planet. If ancient deposits of water-ice indeed still exist, they may preserve atmospheric samples from the past that contain valuable information about Mars's climate history, past atmospheric composition and eventually past life traces. For all such reasons the understanding of the dynamics at the basis of the ice cave phenomena is becoming increasingly important. The computational fluid dynamics (CFD) approach represents a very useful method to investigate the ice cave behavior, as with this technique it is possible, in principle, to simulate the internal air circulation pattern in relation to the external conditions. In the literature, only a few numerical studies of air flow in ice caves have been found ((Yang and Shi (2015),Williams and McKay (2015)), due to the difficulty to obtain the exact geometry of the cave and to set the actual boundary conditions at the domain boundaries. Another challenge is the numerical modellingmodeling of airflow through the limestone-rock, as in complex cave systems air equally flows through the main entrances and the small fractures existing in the rock body. A model of porous material to describe the airflow through these channels is needed. Last but not least, the difficulties to perform air velocity and temperature measurements within the cave, needed for validating the simulations, make the CFD modelization of the ice cave a very challenging problem. The aim of this work is to establish a method for the assessment of ice caves climatology using the Leupa ice cave (LIC) as an example to show how air circulation triggered by temperature and pressure gradients between the inside and the external atmosphere influences ice melting and its maintenance in the cave. The method is based on CFD approach and considers extension of well established techniques developed by some of the authors of this paper to the case of ice cave modelization dealt herein. The methodology takes into account several technical aspects related to domain simplification, grid construction and refinement, boundary-conditions treatments and turbulence closure models choice (Di Sabatino et al. (2007)) (Di Sabatino et al., 2007), as well as the porous media modelization (Buccolieri et al. (2009)) (Buccolieri et al., 2009). The article is organized as follows. Section 2 Section 2 describes the case study, the numerical modellingmodeling methodology and the validation of the numerical data against the measured data. Section 3 Section 3 is devoted to the description of the results. Section 4 Section 3.3 introduces a simplified model to determine the heat exchange between ice and air based on energy balances. Conclusions are outlined in Section 5. Section 4.

2. Study site and methods

2.1. Study site and data description

The Leupa ice cave (LIC) opens at 2285 m asl on the north side of Mt. Leupa (2402 m asl) in the Canin-Kanin group (southeastern Alps; 46° 21′ N, 13° 26′ E) (Fig. 1). Several ice caves are reported in the area with a median elevation of the entrances at 1871 m asl (Colucci et al., 2016) and the landscape is widely characterized by glaciokarst (žebre and Stepišnik, 2015). Dolostones and Limestones of the Norian-Rhetian platform are the prevalent lithologies. LIC hosts a ca. 300 m^3 sub-horizontal and layered ice deposit, averaging ca. 3 m in thickness. The cave is classified as a dynamically ventilated (Perşoiu, 2018) due to the presence of at least three entrances located at different elevations. The middle entrance opens with a 13 m wide and 4 m high gateway. The upper and lower entrances are formed by narrow, unreachable passages and rock fractures. Through the upper entrance, an intense dripping is active from late spring to autumn and major rain events can temporarily flood the cave, inducing superficial melting and the formation of decimetric-in-size supraglacial streams (known as *bediéres*). A few details are known for the bottom shaft, as it is totally filled with by debris accumulation, as shown by geophysical investigation. Then, this shaft is not completely sealed by ice and air is circulating in the debris: this is evident from temperature measurements. Moreover, there is continuation behind the ice, in the opposite direction from the main entrance, that is completely filled by ice. For this reason, we assume that the air flow through that continuation is negligible. At 2200 m asl the 1981–20101981–2010 mean annual air temperature (MAAT) is 1.1 °C ($\sigma = 0.6$), while mean annual precipitation (MAP) is equal to 3335 mm water equivalent (w.e.) (Colucci and Guglielmin, 2015). The precipitation regime is characterized by two peaks in spring and fall (max of 436 mm w.e. in October). High precipitation influences the mean winter snow accumulation which is 7 m at 1830 m asl. The warmest month is July (9.2° C), the coldest February (-6.0–6.0 °C). Thanks to such climatic conditions and the high frequency of avalanches, few small glaciers and ice patches still survive in this area at the foot of the northern rockwalls between 1830-2340 1830 and 2340 m asl (Colucci, 2016), covering a total area in 2012 of 0.14 km^2 with an estimated volume of 0.451 10^3 m^3 (Colucci and žebre, 2016).

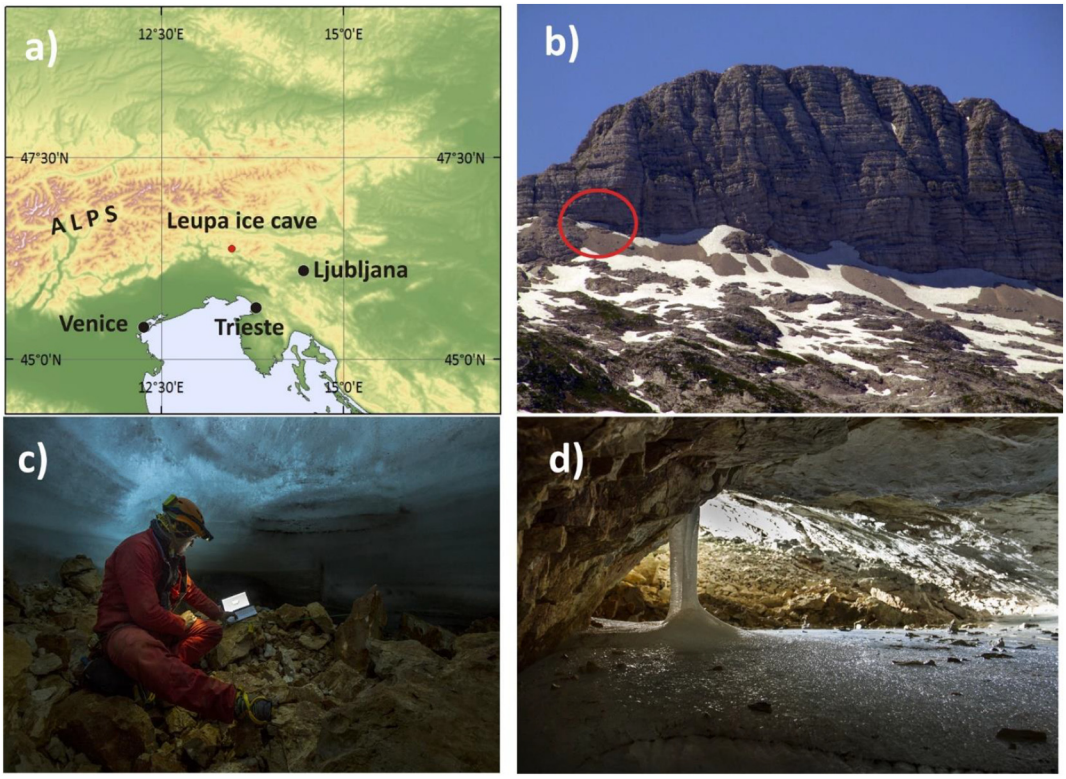

Fig. 1. Overview of the study area and monitored ice cave. (a) Location of the LIC in the southeastern European Alps. This map has been created with the software ArcMap Version 10.1 and is based on digital elevation information from the Shuttle Radar Topography Mission (http://srtm.csi.cgiar.org), further edited by using the CorelDRAW graphic suite, release X3 (http://www.corel.com). (b) The large entrance of the LIC located on the North Face of Mt. Leupa. (c) The dome-shaped melting chamber formed below the ice deposit due to warmer air inflow from the lower entrance. (d) Part of the ice deposit within the LIC as seen from inside towards the main entrance. Photographs are taken by R.R. Colucci.

Microclimatic studies of Leupa ice cave air and rock temperatures are ongoing since 2011. ContinousContinuous monitoring is difficult given the harsh conditions and the impossibility to reach the site during the winter season. Nevertheless, long time-series of air temperature have been acquired with time resolution of 30minutes Colucci et al. (2016) min (Colucci et al., 2016). Fig. 2 shows a longitudinal cross section of the cave and the position of the different sensors installed. Two of the sensors, denoted as TR1 and TR3 measure the rock temperature in two different locations of the cave at a depth of 0.3 m and 1 m respectively. Sensors TA2 and TR3 measure the air temperature and the debris temperature inside a dome-shaped cavity at the bottom of the ice (Fig. 1c), respectively. Sensor TA1 is at 2.1 m from the ice surface, in the middle of the chimney at 2.5 m from othboth sides. TA2 is at 40 cm from the debris surface, surrounded by the ice walls of the dome-shaped room below the ice, at about the same distance as the TA1. TI measures the ice temperature at 0.3 m deep. In correspondence of the middle entrance TR4 monitors the external rock temperature at 0.3 m deep and TA3 measures the temperature at the entrance ceiling. W is a sensor for velocity and air direction measurement. B1-B2 measure the melted ice. The temperature sensors are Tinytag data-loggers TGP4020, equipped with standard thermistor probes PB-5001, whose characteristics are suitable for environmental monitoring. The external temperature is obtained from the Canin Automatic Weather Station, located at 2,200 2200 m asl and 2.4 km East from the LIC main entrance. Being the focus here to simulate the air circulation via numerical modeling, some of the measurements were used as input in the simulations, while the remaining, namely the air temperature values from TA1 and TA2 are used for model verification. An anemometer HOBO-S-WCA-M003 was located inside the LIC, at a distance of 20 m from the main entrance and 30 cm high from the ice surface.

2.2. Numerical modeling

The numerical modeling methodology is organisedorganized in several phases including the domain construction, mesh generation, grid convergency, choice of the turbulence model and validation of the solution by comparison with measured data. The numerical methodology has been developed within Ansys-Fluent 17.2 (http://www.ansys.com/products/fluids/ansys-fluent). The 3D model of the cave has been obtained from a topographic survey performed in 2012 Colucci et al. (2016) on the LIC and from a computer-aided design (CAD) reconstruction. The coordinates of several points in the internal surface of the cave have been measured to extract some contours of vertical and horizontal setions of the accessible part of the cave. With the CAD software Autodesk Inventor (http://www.autodesk.com), the profiles have been used as source contours to obtain different cross sections of the cave. These sections have been swept to form blocks representing the volume occupied by air and ice inside the cave. These blocks have been merged to obtain the total volume of the cave. By interpolating several measurements of the position of the ice boundaries, surfaces delimiting the ice deposit have been reconstructed and used to cut the total volume. In this way, the air filled cavities and ice volume have been obtained. Fig. 3 shows the 3D model obtained by means of the CAD procedure described.

From the 3D model reconstructed as above we estimated a volume of 963 m^3 for air and a volume of 286 m^3 for ice, with maximum extensions in the horizontal directions $L_x = 25$ m and $L_y = 24$ m, while the dimension in the vertical direction is $L_z = 20$ m. This volume, defined as V_{LIC}, represents the accessible part of the LIC and does not include unknown amounts hosted in shafts. Above and below V_{LIC}, two 50 m high cylinders with a diameter of 1 m have been added to model the airflow through the limestone-rock fractures.

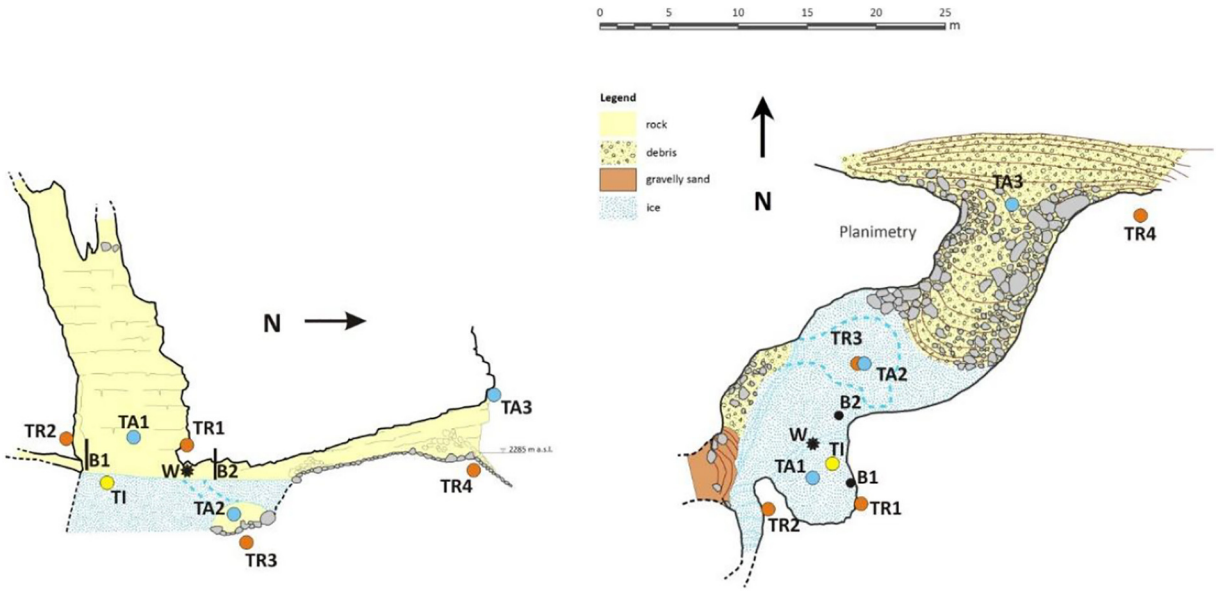

Fig. 2. Map of the ice cave as obtained from measurements and position of the sensors. TR1-TR4 measure the rock temperature, TA1-TA3 measure air temperature, TI measures ice temperature, W measures the air velocity and air direction, B1-B2 measure the ice elevation.

One, V_{up} starts from the uppermost reachable part of the V_{LIC}, while the other, V_{down} starts from the debris floor under the ice. The geometric details of the cave are used as input for CFD modeling, which requires as first step the generation of a suitable mesh needed to solve the flow governing equations. The mesh generation process consists inof the subdivision of the physical volume in cells. Due to the complexity of the cave geometry, meshes with unstructured elements have been created, with hexahedral cells with a finer resolution close to the ice cave inner surface and in those regions where large air velocity gradients are expected. Several tests have been performed to verify grid size independence with increasing number of mesh cells until further refinements gave no significant improvements. The final number of computational cells used for all the simulations was approximately 13 Million million. The smallest dimension of the element was 10^{-8} m^3 in the region near the ice deposit surface. The model proposed in this work solves the Reynolds Averaged Navier-Stokes equations (RANS), by means of Ansys-Fluent 17.2 tool (Di Sabatino et al., 2007). This model is a two-equations model in which the solution of two separate transport equations allows the turbulent velocity and length scales to be independently determined. The following equation is solved for the turbulent kinetic energy k:

$$\frac{\partial \rho k}{\partial t} + \frac{\partial \rho k v_i}{\partial x_i} = \frac{\partial}{\partial x_j}\left[\left(\mu + \frac{\mu_t}{\sigma_k}\right)\frac{\partial k}{\partial x_j}\right] + G_k + G_b - \rho\varepsilon - Y_M + S_k \quad (1)$$

where v_i is the $i-th$ component of air velocity, G_k represents the generation of turbulence kinetic energy due to velocity gradients, G_b is the generation of turbulence kinetic energy due to buoyancy, Y_M represents the contribution of the fluctuating dilatation in compressible

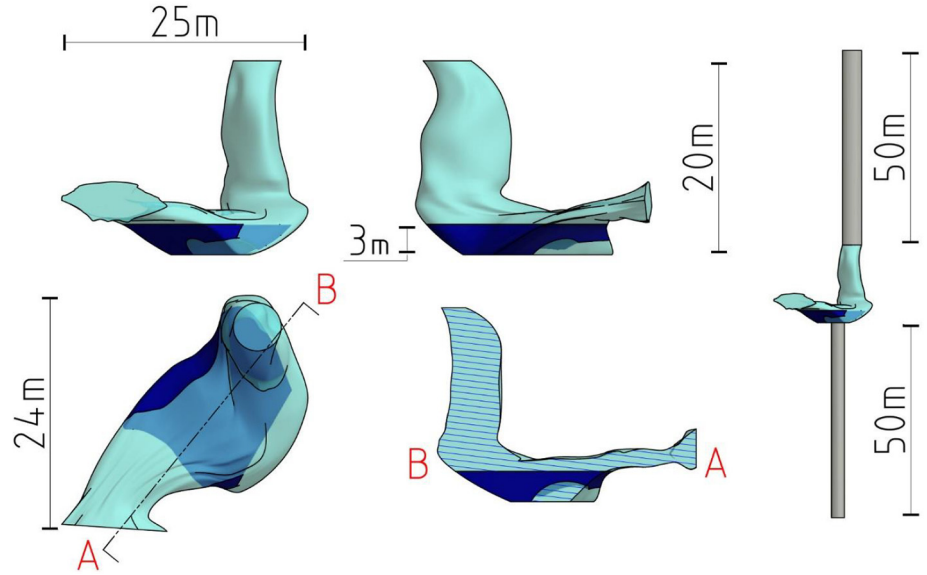

Fig. 3. 3D model of the LIC obtained by means of the CAD procedure. In the four figures on the left the following views are shown: view from the main entrance of the cave (top, left), side view (top, right), top view (bottom, left), section AB shown in the top view (bottom, right). On the right a frontal view of the 3D model of the cave together with the two porous chimneys.

turbulence to the overall dissipation rate and S_k is a source term. The following equation is solved for the rate of dissipation ε

$$\frac{\partial \rho \varepsilon}{\partial t} + \frac{\partial \rho \varepsilon v_i}{\partial x_i} = \frac{\partial}{\partial x_j}\left[\left(\mu + \frac{\mu_t}{\sigma_\varepsilon}\right)\frac{\partial \varepsilon}{\partial x_j}\right] + C_{1\varepsilon}\frac{\varepsilon}{k}(G_k + C_{3\varepsilon}G_b) - C_{2\varepsilon}\frac{\varepsilon^2}{k} + S_\varepsilon \quad (2)$$

where $C_{1\varepsilon}$, $C_{2\varepsilon}$ and $C_{3\varepsilon}$ are constants, σ_k is the turbulent Prandtl number and S_ϵ is a source term. These equations are solved under the Boussinesq approximation for buoyancy, that means that the density is considered as a constant value in all solved equations, except for the buoyancy term in the momentum equation:

$$(\rho - \rho_0)g = -\rho_0 \beta (T - T_0)g \quad (3)$$

where ρ_0 is the fluid density at a reference temperature T_0, g is the gravity constant and β is the thermal expansion coefficient.

The volumes V_{up} and V_{down} represent the two chimneys that connect the accessible part of the LIC to the upper and lower entrances of the cave respectively. They are considered as porous media, i.e. modelled by the addiction of a momentum source term S_i to the standard $i-th$ momentum equation:

$$S_i = -\left(\frac{\mu}{\alpha}\, v_i + \frac{1}{2}\rho c |v|\, v_i\right) \quad (4)$$

where v_i is the $i-th$ component of air velocity, μ and ρ are respectively the air viscosity and density, α is the porous medium permeability and c is a constant related to the porosity γ of the medium. In Eq. (4), the first term represents the viscous loss term, given by the Darcy law and the second term the inertial loss term. To define permeability and porosity, a sensitivity study has been performed, by varying α and γ according to Buccolieri et al. (2009). The final values are $\alpha = 10^{-12}$ m^2 and $\gamma = 0.5$. These values are in agreement with the few data available in the literature (Turk et al. (2014) and Galvão et al. (2016)). Boundary conditions of atmospheric pressure (i.e. zero gauge in the model) and fixed temperature have been imposed at the middle entrance and at the two boundaries at the top and at the bottom of the two porous chimneys, V_{up} and V_{down}. No measures are available at these two boundaries, and even the actual position and shape of these boundaries are unknown. Then, the choice of setting zero pressure boundary conditions has the aim to focus our study only on the investigation of buoyancy induced flow within ice caves. There is no literature on ice caves ventilation by means of CFD approaches. There are some CFD studies about ventilation within mines (Sasmito et al., 2013), but in most of these works velocity boundary conditions are set at the mine entrances, as usually these underground tunnels are ventilated. The two days chosen (6th of January 2012 and the 9th July 2013) showed very stable conditions with uniformity in the temperature distribution with the elevation. The temperature of the air at the upper and lower openings has been set equal to the external temperature measured at the Canin AWS, while the air temperature at the middle entrance has been set equal to the air temperature measured by TA3. The temperature measured 30 cm deep by sensors TR1, TR2, TI1, TR4 and 100 cm deep by sensor TR3 has been imposed at the corresponding depths from the surface boundaries of the volume V_{LIC}. The temperature on the lateral surfaces of the volumes V_{up} and V_{down} has been varied linearly from the value of the external temperature measured by the Canin AWS to the temperature measured by TR1 and TR3 for V_{up} and V_{down}, respectively.

2.3. Verification of the numerical simulations

To investigate airflow dynamics within the cave with a certain degree of confidence, typical scenarios representing the winter and the summer seasons have been considered. The two days chosen to represent the circulation in winter and in summer have been characterised by a measured velocity greater than 0.5 m/s for a time interval longer than 30minutes min, with very stable temperatures. The temperature measured by the sensors during the two days and averaged within the time interval 8-208–20 are shown in Table 1. Boundary conditions at the inner surfaces of the cave have been set equal to the temperature measurements inside the rock, at a distance Δx from the surface. The thermal resistance of the wall is $\Delta x/k_r$, where $k_r = 2.88$ W/(m K) is the thermal conductivity of the rock (Schnepfleitner et al. (2016)) (Schnepfleitner et al., 2016) and $\Delta x = 0.3$ m is the wall thickness for sensors TR1, TR2 and TR4, while $\Delta x = 1$ m is the wall thickness for sensors TR3. Since the measured temperatures refer to a specific location, all the surfaces near each sensor were set to its value. The same approximation has been done for the ice surfaces: the thermal resistance of the wall is $\Delta x/k_i$, where $k_i = 2.2$ W/(m K) is the thermal conductivity of ice and $\Delta x = 0.3$ m is the wall thickness. This choice gives boundary conditions on the ice cave surfaces more adherent to the reality, especially during winter, where temperature distribution is less uniform than during summer. The air temperature at the main entrance has been taken from sensor TA3, while the temperatures at the other two entrances, below and above the ice cave, have been obtained by the Canin AWS measurement. The air temperature obtained by the numerical simulations around the positions of the two inner sensors TA1 and TA2 have been compared with the measurements, respectively above and below the ice deposit. Table 1 shows the averages from the temperatures measured by the sensors during the time interval chosen for the validation.

Fig. 4 (A) shows the temperature distribution obtained numerically for the winter case on the plane where the TA1 sensor is located

Table 1
Temperatures (T) measured by the sensors (averaged on the time interval 8.00–20.00) and standard deviations (STD) during the averaged period.

2*Sensor		Winter case T (°C)	STD (°C)	Summer case T (°C)	STD (°C)
TR1	Rock, 30 cm deep	−2.0 ± 0.4	0.14	0.0 ± 0.4	0.001
TR2	Rock, 30 cm deep	−2.4 ± 0.4	0.13	0.1 ± 0.4	< 0.001
TR4	Rock, 30 cm deep	−1.0 ± 0.4	0.08	0.0 ± 0.4†	0.001
TI1	Ice, 30 cm deep	−3.0 ± 0.4	0.16	−0.1 ± 0.3	< 0.001
TA1	Internal air	−5.8 ± 0.4	0.18	0.0 ± 0.3	0.003
TA2	Internal air	−2.7 ± 0.4	0.3	0.0 ± 0.3	0.002
TR3	Rock, 100 cm deep	−0.5 ± 0.4	0.4	1.4 ± 0.3	0.008
TA3	External air	−7.9 ± 0.4	0.5	6.6 ± 0.3	0.6
T AWS	External air	−10.4 ± 0.3*		13.3 ± 0.3	1.8
Sensor		v (m/s)		v (m/s)	
W	Internal air	0.8 ± 0.3		0.5 ± 0.3	
	Direction (deg)	130 ±10		330 ±10	

† When the sensor TR4 experienced problems the temperature value from TR1 was used as boundary temperature in the numerical model.
*Daily mean value.

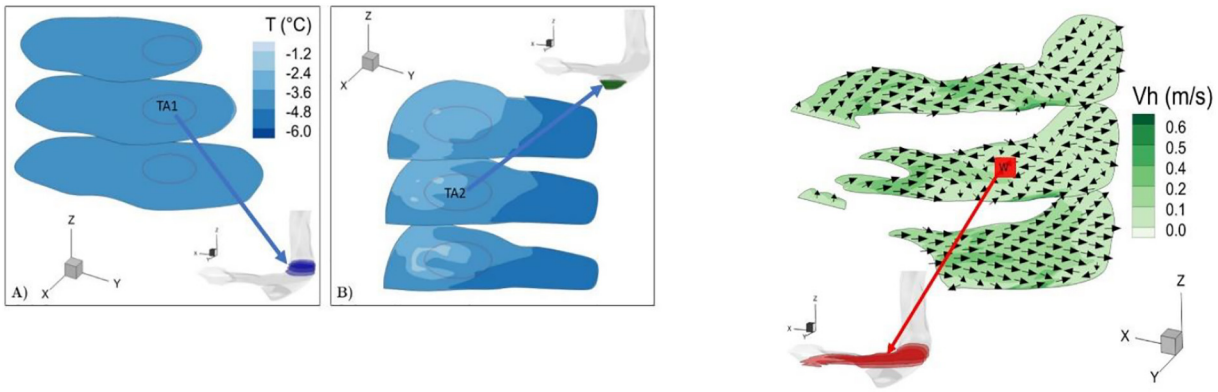

Fig. 4. Temperature distribution obtained numerically for the winter case on the plane where the TA1 sensor is located (middle plane) and in two planes above and below the sensor position (left). Velocity vectors obtained on the plane where the anemometer was located (middle plane) and in the planes 1 cm above and below that plane (right).

(middle plane) and in two planes above and below the sensor position (with a distance of 50 cm between each plane). Panel (B) shows the temperature distribution on horizontal surfaces close to sensor TA2; the lower plane is located 20 cm from the cave floor and 20 cm is the distance between the different planes. The temperature obtained by the numerical simulation in the region above the ice deposit is pretty uniform. The temperature obtained for the position of the sensor TA1 was − 4.4°C, while that obtained for the position of the sensor TA2 was − 2.6°C, then a very good agreement with the measurements has been obtained. These results show that there is a warmer air coming from the bottom of the LIC that remains confined below the ice deposit, while the air flowing above is colder.

Fig. 4 (right) shows the velocity obtained on the plane where the anemometer was located (middle plane) and in the planes 1 cm above and below that plane. The figure shows that the velocity obtained numerically is in the range of the measured velocity, i.e. the velocity obtained in that plane is in the range (0.4 m/s - 0.6 s–0.6 m/s). Moreover, the figure shows that on the two bottom planes the speed is directed almost everywhere towards the interior of the cave, indicating a flow of air that enters the cave. However, in the top and middle planes one can observe a mixing region where the vectors have very different directions. The velocity obtained in then is in agreement with that measured by the anemometer, i.e. 0.8 m/s. A good agreement has been found also for the wind direction obtained by the numerical simulations. In fact, the wind direction measured by the anemometer is, for the winter case, an angle of 130° with the North direction, i.e. the flow is flowing towards the cave interior. From vectors shown by Fig. 4 we can observe that there is a good agreement between the direction obtained in the two lower planes and the experimental measure of the wind direction.

3. Results and discussion

In the dynamically active ice-caves, characterized by multiple entrances at different elevations, the main process controlling the air-exchange between the inside of the cave and the external atmosphere is the so called chimney effect, that is based on differences in internal and external air density. During winter the internal air, that is warmer and less dense than the external one, flows out from the upper entrances due to its buoyancy, while colder air from the outside is sucked inside the cave from the lower entrances. During summer the process is reversed, i.e. the cave air is colder and denser than the external one and tends to move down, forcing outside warmer air from the upper entrances. As described above, the LIC is characterized by a main entrance at about the same elevation of the ice deposit, while upper and lower entrances are unknown, but expected to be smaller and characterized by higher flow resistances. Therefore, more complex dynamics is expected in the region near the main entrance where the ice is located. In the channel connecting the main entrance to the cave two airflows with opposite directions and different temperatures are expected, as shown by Fig. 5. In winter conditions (left in the figure), warmer air coming from the bottom of the cave is expected to flow towards the main entrance. This flow is expected to occupy the upper part of the channel, while colder external air enters in the cave through the bottom part of the channel. In summer conditions (right in the figure), colder air coming from the upper part of the cave is expected to flow towards the main entrance. This flow is expected to occupying the lower part of the channel, while warmer external air enters in the cave through the upper part of the channel.

Both in winter and in summer conditions, two opposite flows of air with different temperatures intersect and mix near the ice deposit. Understanding the airflow pattern and circulation in that region is then very crucial in order to understand the heat transfer mechanism near the ice surface. The lines showing air flow within the ice cave in Fig. 5 appear to pass through the ice body. Indeed, air flows within a narrow path between the ice and the rock surface (right to the ice body in the figure). This detail is not shown by the figure as the scope is to show the shear flows above the ice body near the middle opening of the cave. Two cases have been considered to underline these aspects and to characterize the structure of the airflow in winter and in summer. The two cases are described in Section 2.3 Section 2.3 and the boundary conditions are shown in Table 1 Table 1, where the sensors TR1, TR2, TR3, TR4, TI1 have been used to set the temperature at the inner surface of the ice cave; while air temperature data from TA3 and Canin AWS have been used to set the temperature at the different entrances of the cave. The results obtained from the numerical simulations for winter and summer are discussed as follows.

3.1. Winter circulation

The expected winter air circulation within a dynamically active ice cave consists of an upward flow due to the rising of the warmer internal air. The flow of colder air coming from the lower entrance rises upwards, attracted by the air that has been heated up in contact with the rock and the ice. The warmer air then exits by the upper openings. In the case of LIC, as the ice deposit is at the same level of the middle opening of the cave, a difference in the circulation at the channel connecting that opening to the cave can be expected. The streamlines obtained by the simulations confirm these expectations, as shown by Fig. 6, where the streamlines are colored with the temperature of air.

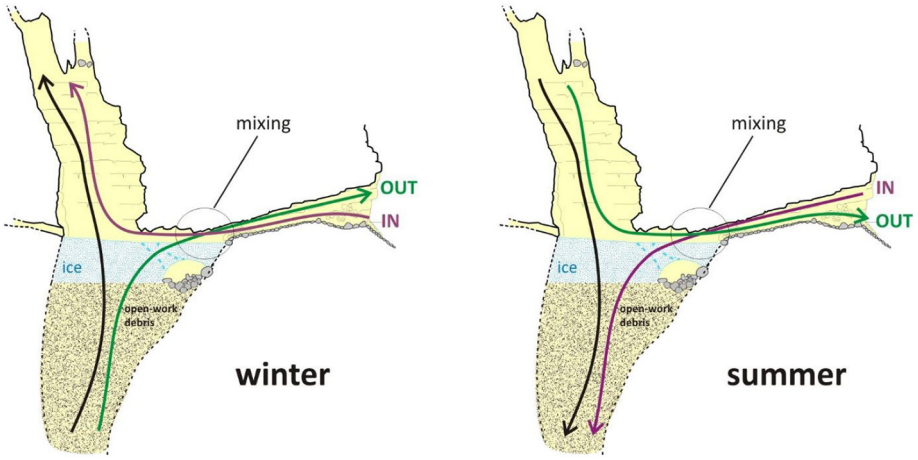

Fig. 5. Scheme of the airflows within the LIC. Left: winter circulation. Right: summer circulation.

Fig. 6 shows that the warmer air coming from the channel under the ice is divided into two flows, one directed towards the middle opening of the cave and one directed upwards. Moreover, in the zone under the ice deposit, two recirculation vortices are observed, which actually can contribute in shaping the ceiling of the melting chamber at the base of the ice deposit. Some important features characterizing the cave thermal behavior during winter can be therefore summarised as follows.

- The temperature of chimneys surfaces is fairly uniform, while near the main entrance the temperature obtained on the surface is not uniform, i.e. in the upper part the surface temperature is warmer than in the lower part. This is due to the layer or warmer air exiting towards the middle opening and flowing in the upper part of the channel.
- The temperature difference between the ice surface near the inlet and at the base of the chimney is about 2.5 °C.
- The air flow through the middle opening is stratified: the warm air rising from below is in the upper part of the channel near the entrance, while the cold air that enters from this opening is in the lower part of the channel.
- The flow recirculation pattern in the cavity below the ice deposit is consistent with the shape of the bottom surface observed in the ice.

3.2. Summer circulation

The expected summer air circulation within a dynamically active ice cave consists of a downward flow of air coming from the upper openings with a higher density after the contact with the ice and the rock. The cool air exits by the lower opening. In the case of LIC, as the ice deposit is at the same level of the middle opening of the cave, a difference in the circulation at the channel connecting that opening to the cave is expected.

Fig. 7 shows that air flowing in the channel above the ice is divided into two shear flows, one directed towards the middle opening of the cave and coming from that opening and directed to the ice cave interior. In the zone above the ice deposit, a recirculation of the airflow coming from the main entrance is observed. Some important features characterizing the cave thermal behavior can be summarized as follows.

- The temperature of chimney walls is fairly uniform, while near the entrance the upper part is warmer. This is due to the layer of warmer air entering from the middle opening and flowing in the upper part of the channel.
- The temperature difference between the ice surface near the inlet and at the base of the chimney is about 5 °C.

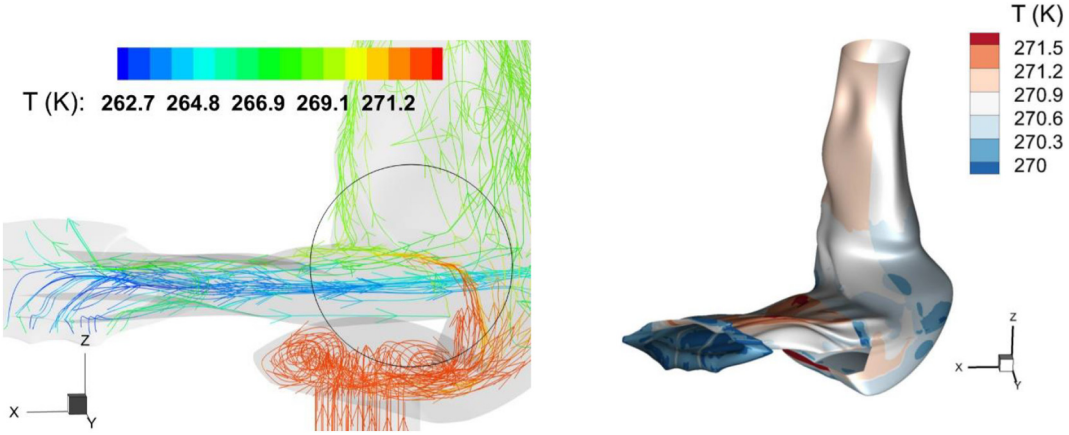

Fig. 6. Streamlines colored with temperature (left) and temperature on the ice cave surface (right) obtained for the winter case.

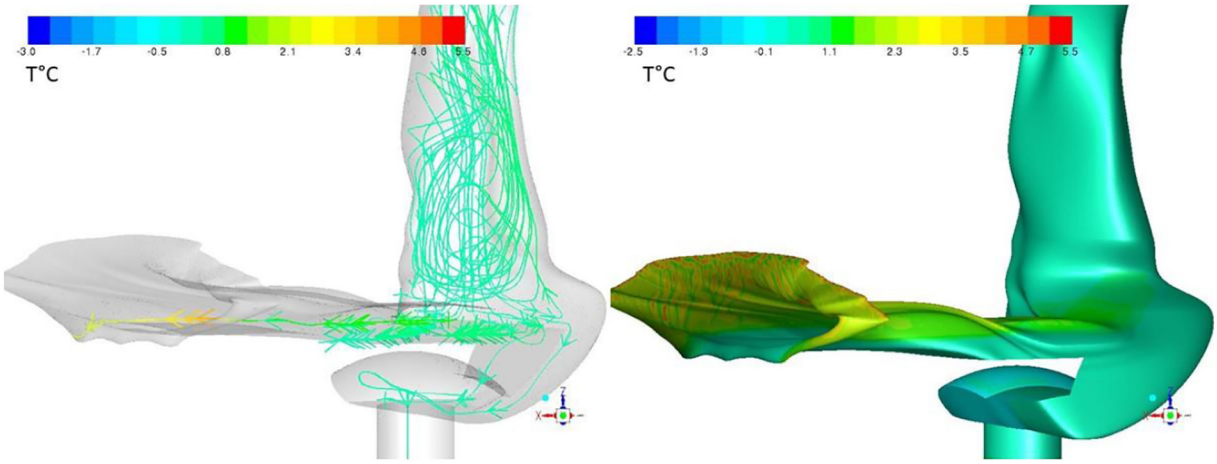

Fig. 7. Streamlines colored with temperature (left) and temperature on the cave surface (right) obtained for the summer case.

- The warm air that falls through the upper chimney mostly exits through the main entrance.
- Flow recirculation above the ice deposit under the upper chimney could enhance the ice melting in that zone, while the stagnation region just near that vortices produce a colder zone where ice can be preserved.

3.3. Modeling of the ice melting mechanism

In this section, a model for the ice melting within the cave is yield, based on the assumption that the ice melting is due mainly to the heat transfer between the air flowing within the cave and the ice surface. The radiation heat transfer from the cave inner surfaces to the ice is neglected. This choice is supported by the measurements, showing that for long periods during summer the rock internal surfaces above the ice have the same temperature as the ice surface, i.e. in these days the heat exchanged by thermal radiation is negligible. From the numerical results it is possible to obtain the local heat flux at the air-ice interface, $\dot{q}$, as follows:

$$\dot{q} = -\rho c_p(\alpha + \alpha_t)\frac{\partial T}{\partial n} \tag{5}$$

where ρ and c_p are respectively density and specific heat of air, α is the thermal diffusivity and $\alpha_t = \frac{\nu_t}{Pr_t}$ is the eddy diffusivity, T is the temperature and n is the normal to the surface. By a local energy balance between the airflow and a small portion of ice surface δS, during a time interval δt

$$\dot{q}\delta t\delta S = h_{sl}\delta m + c_p\delta T\delta m, \tag{6}$$

where $h_{sl} = 334$ (kJ/kg) is the water specific latent heat of fusion at standard pressure, $\delta T = T - T_0$, with $T_0 = 273$ K and $c_p = 2.108$ kJ/(kg K) is the specific heat of ice. From Eq. (6) one can obtain the mass δm of ice melted locally, during the time interval δt:

$$\delta m = \frac{\dot{q}\ \delta t\ \delta S}{h_{sl} + c_p\ \delta T} \tag{7}$$

Fig. 8 shows the local heat flux to the ice surface for the conditions shown in Section 3.3 Section 3.3. The local heat flux is in the interval $(-1.2 - 0.1)$ W/m^2, where negative values mean that the heat flux is transferred to the ice layer. Figure shows that the highest negative values for the heat flux are observed where the warm air is flowing. These are the region where a stronger ice melting ice is expected locally.

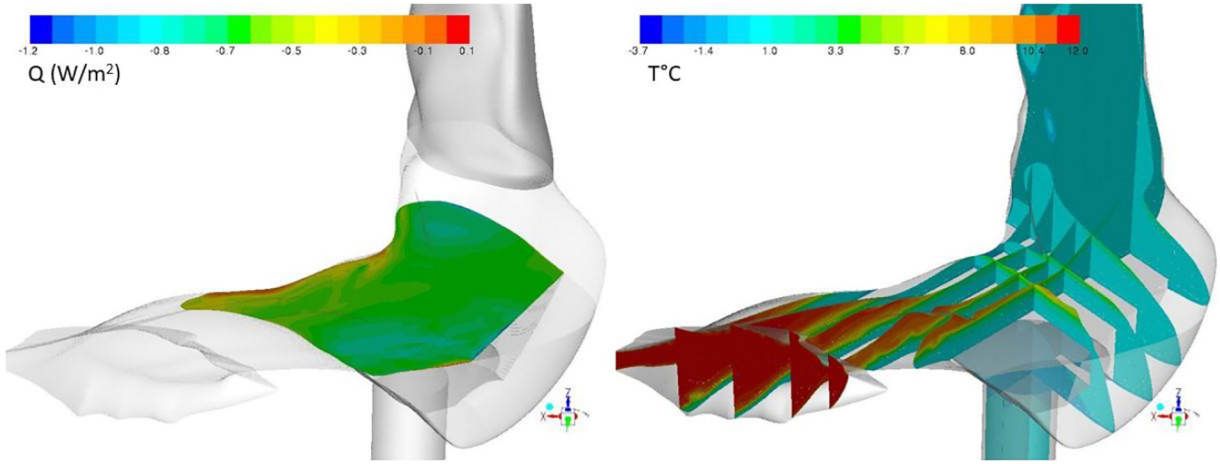

Fig. 8. Local heat flux on the ice surface (left) and air temperature on vertical planes (right) obtained for the summer case.

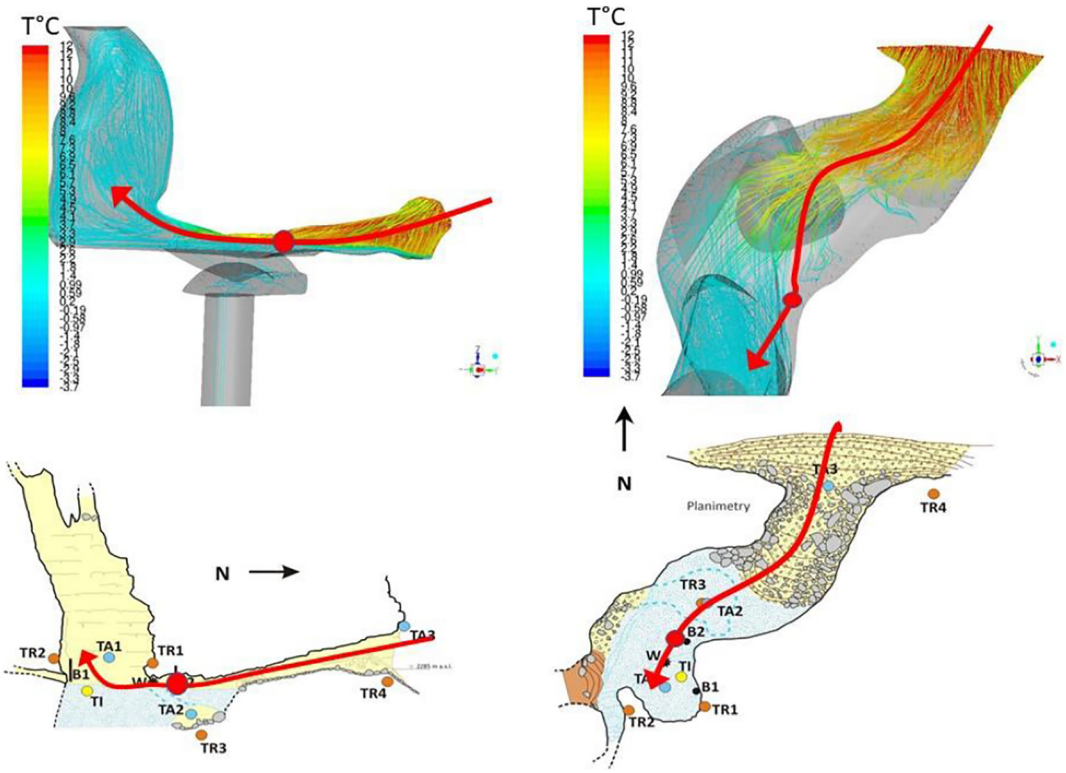

Fig. 9. Scheme of the main air flux within the cave during summer conditions.

From these results it is interesting to obtain some dimensionless number typical for natural convection problems, as the Rayleigh number

$$\mathrm{Ra} = \frac{\beta g L^3 \Delta T}{\mu k} \tag{8}$$

where β is the thermal espansionexpansion coefficient and L is a characteristic length for the case considered. For the case considered in this section, $\Delta T = T_{air} - T_{ice} = 7$, then the average temperature is $T_{av} = (T_{air} + T_{ice})/2 = 276$ K and $\beta = 1/T_{av} = 0.0036$ K^{-1}. At T_{av}, the air viscosity is $\mu = 1.81 \times 10^{-5}$ Pa s and the thermal conductivity is $k = 0.026$ W/(m K). By choosing as a characteristic length the ice body horizontal length, $L \sim 20$ m, we obtain Ra$= 4.2 \times 10^{10}$. Fig. 9 shows a scheme of the air flowing from the main entrance to the inner ice cave during summer conditions. The quantity of melted ice is affected by a very high non uniform distribution, depending of the local heat transfer with the air flowing within the cave, above the ice surface. The positions of the two points where the ice body levels have been measured are highlighted in Fig. 9 (B1 and B2).

Fig. 10 shows the thickness of the melted ice measured at locations B1 and B2 from September 2011 (the positions of B1 and B2 are shown in Fig. 2). In Fig. 10, the x axis represents the time, starting from August 2011. The black circle is centered on the measured values during November 2013, *i.e.* after the summer 2013. The figure shows that, during summer 2013, the amount of melted ice is larger in position B1 than in position B2. This result is confirmed by numerical simulations, where a higher heat exchange has been obtained on the ice-air interface near position B1.

The measured average thickness of melted ice during summer 2013 is about 4 cm. By considering a small thickness of ice on surface δS, the mass of melted ice can be expressed as $\delta m = \rho\, \delta S\, \xi$, where

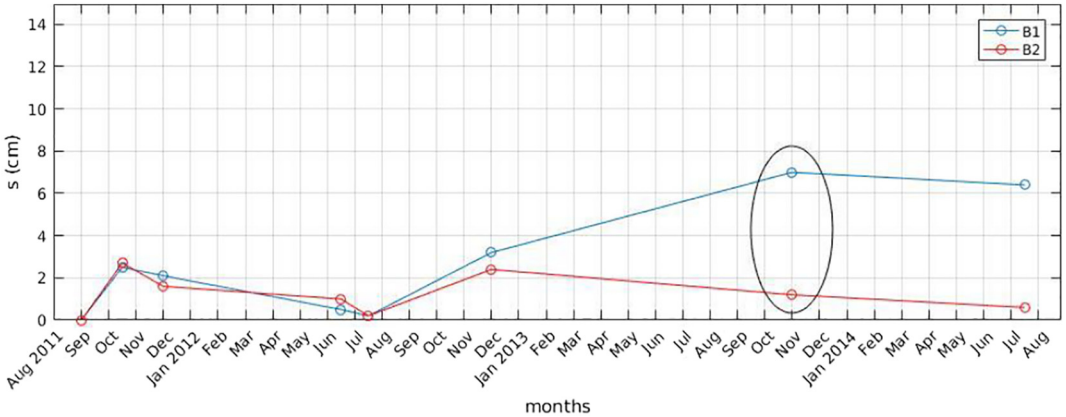

Fig. 10. Thickness of the melted ice.

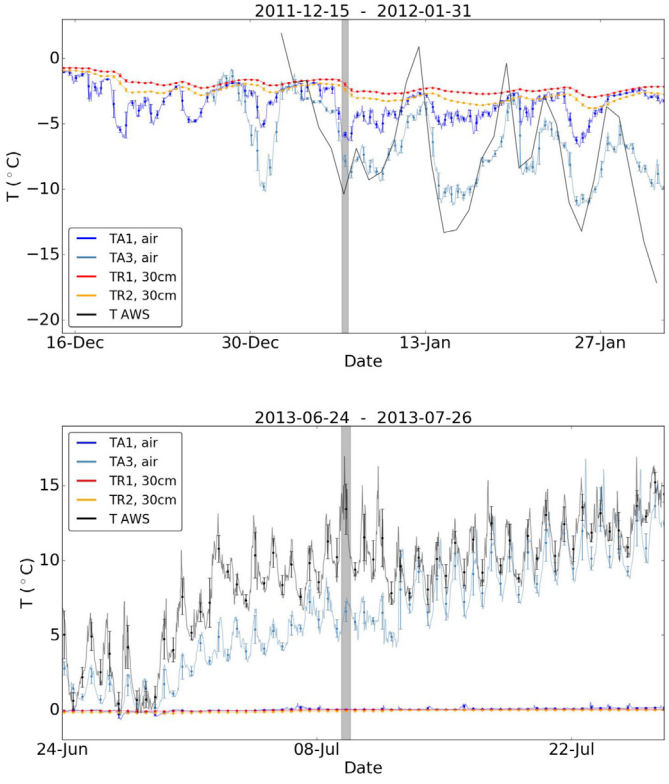

Fig. 11. Temperature measurements within LIC.

$\rho_i = 917$ kg/m^3 is the density of ice and ξ is the thickness of melted ice. Then, from Eq. (7) it is possible to obtain the local thickness of melted ice, as

$$\xi = \frac{\dot{q}\ \delta t}{\rho_i(h_{sl} + c_p\ \delta T)} \tag{9}$$

By averaging ξ over the total surface and by integrating over time Eq. (9) one can obtain the average thickness of melted ice on the top surface of the ice body per day, i.e. $\xi \sim 0.5$ mm per day. Integrating this value over the period in summer 2013, characterized by temperature differences similar to the ones considered in the test case shown in this paper, we obtain an average thickness of melted ice $s_{av} = 4$ cm for the summer 2013. This result is in very good agreement with the measurements. We can conclude that, even the model herein presented is based on very trivial assumptions, it can give a rough estimation of the melted ice thickness within the ice cave, both locally and by averaging over the total surface.

3.3.1. Sensitivity analysis

Fig. 11 shows the average air and rock temperatures measured within the LIC during the period 2011-2017 2011–2017, together with the interval of variation of these measurements. By varying the temperatures within the intervals shown by Fig. 11 we have obtained the range covered by the results obtained in the previous section, i.e. a sort of uncertainty for the melt induced change of surface height within the ice cave.

We obtain a root mean square deviation for ξ RMSD=0.1 mm and for s_{av} we obtain a root mean square deviation RMSD=2 cm.

4. Conclusions

Several mechanisms contribute to the determination of the ice cave microclimate: the airflow pattern, the intrusion of water, the geothermal flux and the radiative contribution. Of these mechanisms, it is interesting to understand which role is played by the air circulation. In this paper, the ice cave has been considered as mainly driven by buoyancy forces. A novel Computational Fluid Dynamics (CFD) model approach has been presented, to give a quantitative description of the phenomena that can govern cave's microclimate under some conditions. This approach has been complemented by a physics-based model of heat and mass exchanges at the ice-air interface. Using the methodology framework introduced in this paper we have shown characteristics of airflow and temperature distribution driven by external forcing. Differently from available studies in the literature we focus on the three dimensionality of the geometry, relevant for not to loose knowledge about the localization of flow stagnation and recirculation zones, spatial variability of the air temperature distribution. We apply this method to the Leupa Ice Cave (LIC), characterisedcharacterized by a main entrance at about the same level of the permanent inner ice deposit. Via the CFD analyses we show that both in winter and in summer the main entrance is exposed by two types of circulation: a cold one affecting the lower part of the entrance and a warmer one in the upper part of the entrance. In the region close to the main entrance and near to the ice deposit, recirculation regions and mixing between the two flows have been observed. The three-dimensional localization of the flow structures give important information about the zones characterised by high energy fluxes between air and ice surface and ice melting phenomena. We showed that using a physics-based heat transfer model locally applied in the stagnation regions it is possible to estimate the rate of ice melting in the cave. Using validated CFD simulations for the LIC we found that a decrease of ice thickness of 4 cm/year and larger should be expected for this cave. These results are in good agreement with the measurements of decrease of ice thickness made in 2013 in the LIC. The methodology framework proposed in this paper can be extended to other ice caves and applied taking into account predictions of air forcing in climate change scenarios and allowing more robust calculations of climate feedback.

Author contributions

R.R.C. and S.D.S conceived this study. B.B. and R.R.C. analyzed the temperature data. B.B., B.P. and S.D.S. set up the numerical approach and methodology. All the authors equally contributed in discussing the results and writing the manuscript.

Acknowledgments

This research was realized within the framework of the "C3 - Cave's Cryosphere and Climate" project (www.c3project.net) thanks to the "E.Boegan" Caves Commission of the Societá Alpina delle Giulie (SAG-CAI), and in the framework of the agreement N.1035 08/02/2017 between the ISMAR-CNR and the SAG. The instrumentation was made available thanks to the Unione Meteorologica del Friuli Venezia Giulia through a financial support from the Comunitá Montana del Gemonese, Canal del Ferro e Valcanale.

References

Behm, M., Dittes, V., Greilinger, R., Hartmann, H., Plan, L., Sulzbacher, D., 2009. Decline of cave ice — a case study from the Austrian Alps (Europe) based on 416 years of observation. Proc. 15Th Intern. Congr. Speleol., Kerrville, Texas, 19 26 July. pp. 1413–1416.

Buccolieri, R., Gromke, C., Di Sabatino, S., Ruck, B., 2009. Aerodynamic effects of trees on pollutant concentration in street canyon. Sci. Total. Environ. 407, 5247–5256.

Colucci, Renato R., 2016. Geomorphic influence on small glacier response to post-little ice age climate warming: Julian alps, Europe. Earth Surf. Process. Landf. 41 (9), 1227–1240. ISSN 10969837. https://doi.org/10.1002/esp.3908.

Colucci, R.R., Fontana, D., Forte, E., Potleca, M., Guglielmin, M., 2016. Response of ice caves to weather extremes in the southeastern Alps, Europe. Geomorphology 261, 1–11. ISSN 0169555X. https://doi.org/10.1016/j.geomorph.2016.02.017.

Colucci, Renato R., Guglielmin, Mauro, 2015. Precipitation-temperature changes and evolution of a small glacier in the southeastern European Alps during the last 90 years. Int. J. Climatol. 35 (10), 2783–2797. ISSN 1097-0088. https://doi.org/10.1002/joc.4172.

Colucci, Renato R., Luetscher, Marc, Forte, Emanuele, Guglielmin, Mauro, Lenaz, Davide, Principalle, Francesco, Vita, Francesca, 2017. First alpine evidence of in situ coarse cryogenic cave carbonates (CCCCOARSE). Geografia Fisica e Dinamica Quaternaria 40 (1), 53–59. ISSN 03919838. https://doi.org/10.4461/GFDQ2017.40.5.

Colucci, Renato R., žebre, Manja, 2016. Late Holocene evolution of glaciers in the southeastern Alps. Journal of Maps ISSN 17445647. https://doi.org/10.1080/17445647.2016.1203216.

Di Sabatino, S., Buccolieri, R., Pulvirenti, B., Britter, R., 2007. Simulations of pollutant dispersion within idealised urban-type geometries with CFD and integral models. Atmos. Environ. 41, 8316–8329.

Frederick, R.D., Billings, T.L., Mc Gown, R.D., Walden, B.E., 2000. Martian ice caves. Workshop on Concepts and Approaches for Mars Exploration (Houston, Texas, July 2000).

Galvão, P., Halihan, T., Hirata, R., 2016. The karst permeability scale effect of Sete Lagoas, MG, Brazil. Journal of Hydrology https://doi.org/10.1002/hyp.10313.

Hausmann, H., Behm, M., 2011. Imaging the structure of cave ice by ground-penetrating radar. Cryosphere 5 (2), 329–340. ISSN 19940416. https://doi.org/10.5194/tc-5-329-2011.

Holmlund, Per, Onac, Bogdan P., Hansson, Margareta, Holmgren, Karin, Morth, Magnus, Nyman, Mart, Persoiu, Aurel, 2005. Assessing the palaeoclimate potential of cave glaciers: the example of the scarisoara ice cave (romania). Geografiska Annaler, Series A: Physical Geography 87 (1), 193–201. ISSN 04353676. https://doi.org/10.1111/j.0435-3676.2005.00252.x.

Kern, Z., Szeles, E., Horvatincic, N., Forizs, I., Bocic, N., Nagy, B., 2011. Glaciochemical investigations of the ice deposit of Vukusic Ice Cave, Velebit Mountain, Croatia. Cryosphere 5 (2), 485–494. ISSN 19940416. https://doi.org/10.5194/tc-5-485-2011.

Luetscher, M., Borreguero, M., Moseley, G.E., Spötl, C., Edwards, R.L., 2013. Alpine permafrost thawing during the Medieval Warm Period identified from cryogenic cave carbonates. Cryosphere 7 (4), 1073–1081. ISSN 19940416. https://doi.org/10.5194/tc-7-1073-2013.

Luetscher, Marc, Jeannin, Pierre Yves, 2004. A process-based classification of alpine ice caves. Theoretical and Applied Karstology 17 (January 2004), 61–66.

Luetscher, M., Jeannin, P.Y., Haeberli, W., 2005. Ice caves as an indicator of winter climate evolution: a case study from the Jura Mountains. The Holocene 15 (7), 982–993. ISSN 09596836. https://doi.org/10.1191/0959683605hl872ra.

Luetscher, Marc, Lismonde, Baudouin, Jeannin, Pierre Yves, 2008. Heat exchanges in the heterothermic zone of a karst system: Monlesi cave, Swiss Jura mountains. Journal of Geophysical Research: 113 (2), 1–13. ISSN 21699011. https://doi.org/10.1029/2007JF000892.

Maggi, Valter, Colucci, Renato R., Scoto, Federico, Giudice, Gaetano, Randazzo, Luca Giovanni, 2018. Ice caves in Italy. In: A., Perşoiu, Stein.Erik, Lauritzen (Eds.), Ice Caves. Elsevier, pp. 750.

Obleitner, F., Spotl, C., 2011. The mass and energy balance of ice within the Eisriesenwelt cave, Austria. Cryosphere 245–257. https://doi.org/10.5194/tc-5-245-2011.

Oliva, M., žebre, M., Guglielmin, M., Hughes, P.D., Çiner, A., Vieira, G., Bodin, X., Andrés, N., Colucci, R.R., García-Hernández, C., Mora, C., Nofre, J., Palacios, D., Pérez-Alberti, A., Ribolini, A., Ruiz-Fernández, J., SarÃśkaya, M.A., Serrano, E., Urdea, P., Valcárcel, M., Woodward, J.C., YÃśldÃśrÃśm, C., 2018. Permafrost conditions in the Mediterranean region since the Last Glaciation. Earth-Science Rev. 185 (June), 397–436. ISSN 00128252. https://doi.org/10.1016/j.earscirev.2018.06.018.

Perşoiu, A., 2018. Ice caves climate. In: A., Perşiou, Stein.Erik, Lauritzen (Eds.), Ice Caves. Elsevier, pp. 750.

Perşoiu, Aurel, Onac, Bogdan P., 2012. Ice in caves. In: David, Culver (Ed.), Encyclopedia of Caves. Academic Press, pp. 399–404.

Sasmito, A., Bigersson, E., Ly, H., Mujumdar, A., 2013. Some approaches to improve ventilation system in underground coal mines environment– a computational fluid dynamic stud. Tunneling and Underground Space Technology 34, 82–95.

Schnepeitner, H., Rode, M., Sass, O., 2016. Validation of simulated temperature profiles at rock walls in the Eastern Alps (Dachstein). Permafrost and Periglacial Processe 1–15. https://doi.org/10.1002/ppp.1962.

Spötl, C., Cheng, H., 2014. Holocene climate change, permafrost and cryogenic carbonate formation: insights from a recently deglaciated, high-elevation cave in the Austrian Alps. Clim. Past 10 (4), 1349–1362. ISSN 18149332. https://doi.org/10.5194/cp-10-1349-2014.

Stoffel, Markus, Luetscher, Marc, Bollschweiler, Michelle, Schlatter, Frederic, 2009. Evidence of NAO control on subsurface ice accumulation in a 1200 yr old cave-ice sequence, St. Livres Ice Cave, Switzerland. Quatern. Res. 72 (1), 16–26. ISSN 00335894. https://doi.org/10.1016/j.yqres.2009.03.002.

Turk, J., Malard, A., Jeannin, P., Petrič, M., Gabrovšek, F., Ravbar, N., Voillamoz, J., Slabe, T., Sordet, V., 2014. Hydrogeological characterization of ground water storage and drainage in alpine Karst aquifer (the Kanin Massif, Julian Alps. Hydrological Processes https://doi.org/10.1002/hyp.10313.

Williams, K.E., McKay, Christopher P., 2015. Comparing flow-through and static ice cave models for shoshone ice cave. Int. J. Speleol. 44 (2), 115–123. ISSN 1827806X. https://doi.org/10.5038/1827-806X.44.2.2.

Williams, K.E., McKay, Christopher P., Toon, O.B., Head, James W., 2010. Do ice caves exist on Mars? Icarus 209 (2), 358–368. ISSN 00191035. https://doi.org/10.1016/j.icarus.2010.03.039.

Yang, S., Shi, Y., 2015. Numerical simulation of formation and preservation of Ningwu ice cave, Shanxi, China. Cryosphere 1983–1993. https://doi.org/10.5194/tc-9-1983-2015.

Žebre, Manja, Stepišnik, UroÅą, 2015. Glaciokarst landforms and processes of the southern Dinaric Alps. Earth Surf. Process. Landf. 40 (11), 1493–1505. ISSN 10969837. https://doi.org/10.1002/esp.3731.